Research Article Vol. 10, No. 6 | 1 Jun 2019 | BIOMEDICAL OPTICS EXPRESS 2861

Biomedical Optics EXPRESS

Structured illumination Mueller matrix imaging

JOSEPH P. ANGELO, THOMAS A. GERMER,* AND MARITONI LITORJA

Sensor Science Division, National Institute of Standards and Technology, 100 Bureau Drive, Gaithersburg, MD 20899, USA
**thomas.germer@nist.gov*

Abstract: We perform Mueller matrix imaging (MMI) of diffusely scattering phantoms under sinusoidal irradiance of varying spatial frequency. Quantitative polarimetric sensing via MMI completely characterizes a sample's polarimetric properties, while structured illumination (SI) allows for the control of photon path length. Intralipid phantoms were measured with varying absorption and with varying depth to demonstrate photon path length control for Mueller matrix elements. We observe unpolarized intensity, linear polarization, and circular polarization to depend upon spatial frequency differently. Finally, we measured an *ex vivo* chicken skin sample over a bright and dark substrate to further demonstrate the sensitivity of SI-MMI to depth.

1. Introduction

Mueller matrix imaging (MMI) has received special attention for its wide-field, quantitative, and complete measure of a sample's polarimetric properties [1]. Polarimetry techniques have been shown to be sensitive to changes in particle size distribution [2], absorption [3], and tissue anisotropy [4], all of which can contribute to contrast between healthy and diseased tissue [1,5,6]. While the field is rapidly expanding, work remains to make MMI robust enough for bulk tissue measurements. Elements of the Mueller matrix (MM) and its associated polarimetry parameters, such as depolarization [7], are sensitive to optical variations associated with disease [5], yet variations in absorption or tissue thickness unrelated to disease can confound the imaging signal [6]. It is also expected that different polarization states propagate through tissue differently, suggesting that analysis of Mueller matrix propagation length scales can add contrast mechanisms not observable with unpolarized optical modalities.

There is interest in sensing both deep and superficial tissue malignancy [1]. In diffuse media, absorption can have a complicated effect on the polarization parameters [3], a direct result from the shortening of the average photon path length. Thus, groups have attempted depth-sensitive polarimetry measurements, but these are either difficult to interpret due to confounding factors (spectral gating [6]) or difficult to implement for wide-field imaging (coherence gating [8]). Recent work has demonstrated a new way of controlling photon penetration depth on a macroscale by using structured illumination (SI) (spatial frequency gating [9,10]) to enable microscopic scattering contrast over a macroscopic field of view. SI and MMI are capable of being wide-field, quantitative, inexpensive techniques that can potentially be synergistically combined to improve accuracy and understanding of tissue optical properties and how they relate to tissue viability.

In this letter, we combine structured illumination with Mueller matrix imaging to make a system that is sensitive to the polarization dependence of the optical path length. Bulk tissue phantoms of varying absorption and scattering are measured to explore spatial frequency and optical property dependence. We then measure an optical step phantom to examine the effect of penetration depth with increasing spatial frequency. Finally, an *ex vivo* chicken skin sample with a heterogeneous substrate is measured to demonstrate depth sensing control.

2. Methods

Mueller matrix polarimetry has been extensively studied in the past [1]. The polarization state of a paraxial beam can be described as a four-element Stokes vector, and the scattering

#359878 https://doi.org/10.1364/BOE.10.002861
Journal © 2019 Received 12 Feb 2019; revised 7 May 2019; accepted 8 May 2019; published 16 May 2019

Biomedical Optics EXPRESS

interaction between incident and outgoing Stokes vectors can be represented by a 4 × 4 Mueller matrix **M**. In practice, **M** is determined by exposing the sample with several (at least four) linearly independent Stokes vectors. The system presented here is based on the liquid crystal (LC) polarimeter developed by De Martino et al. [11] and uses two pairs of LC variable retarders. This design was chosen because the optics have a large clear aperture, are compact, rapidly switch between states, and lack moving parts. We use the eigenvalue method [12] to calibrate the system on the optical axis. To validate the system's polarimetric accuracy, we measured the transmittance of a Glan-Thompson linear polarizer at rotated angles from 0° to 180° every 10° and reflectance from a 1000 nm SiO_2/Si reference at 40°, 50°, and 60° angles of incidence. The results of these measurements demonstrate that systematics in measurements of the normalized Mueller matrix elements along the optical axis contribute a standard uncertainty of 0.02.

A review of structured illumination in diffuse optics can be found in Ref [13], and only a brief summary is presented here. The system illuminates the sample with a sinusoidal intensity pattern with a spatial frequency f_y. Uniform illuminated reflectance ($f_y = 0$) from turbid media has contributions from a wide distribution of photon path lengths, singly and multiply scattered photons, and is therefore sensitive to both absorption and scattering phenomena. However, increasing the illumination spatial frequency shortens the average photon path length associated with the modulated reflectance, resulting in shallower depth of penetration, loss of sensitivity to absorption, and increased sensitivity to scattering phase function parameters [9,14]. Depth sensitivity obtained by SI results from the rapid reduction of intensity modulation that exists for high spatial frequency as the radiation scatters through the material.

The system generates structured illumination with a digital light processing (DLP) engine, utilizing a light-emitting diode (LED) with wavelength centered at 630 nm with a full width at half maximum of 17 nm (see Fig. 1(a)). The angle between the illumination and collection optical axes is approximately 20°, and the collection optical axis coincides with the sample surface normal. The sample is imaged with a 35 mm focal length objective onto a 1024 × 1024 CCD camera with 2 × 2 pixel binning for 512 × 512 pixel-resolution images. The system has a full field of view (FOV) of 9 cm × 9 cm, though all samples presented here are within 6 cm × 6 cm.

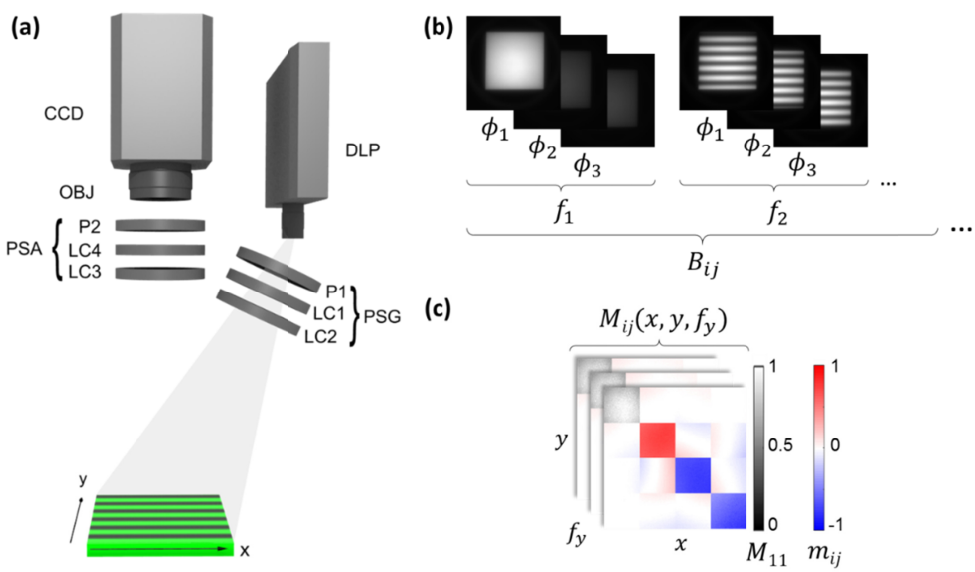

Fig. 1. Outline of (a) system schematic, (b) acquisition scheme, and (c) sample data mapping.

Biomedical Optics EXPRESS

For each sample, the following acquisition sequence was used to build a 4 × 4 set of raw images **B** (with elements B_{ij}) (see Fig. 1(b)) for each spatial frequency to calculate $\mathbf{M}(f_y)$ [with elements $M_{ij}(f_y)$] (see Fig. 1(c)). The polarization state generator (PSG) generates four independent states (index $i = 1,\ldots,4$), while the polarization state analyzer (PSA) analyzes four states (index $j = 1,\ldots,4$), creating the 16 elements of **B**. The MM calibration procedure creates the relationship between **B** and **M** [12]. For each spatial frequency, three images are projected at phases $\varphi = [0°, 120°, 240°]$ and imaged for demodulation to retrieve the spatial-frequency-dependent reflectance [14]. As depicted in Fig. 1(b), a set of spatial frequencies from 0 mm^{-1} to 1 mm^{-1} in steps of 0.1 mm^{-1} (11 total) was collected for every element of **B**, and every spatial frequency had three phases collected for demodulation [14]. Two repetitions were acquired and averaged for every sample unless otherwise stated. Thus, the total number of images acquired for each sample was 11 × 16 × 3 × 2 = 1056.

The raw data were then corrected in two ways: (a) the modulation transfer function (MTF) was determined by measuring a rough aluminum reference, which, as a surface scatterer with no appreciable diffusive scattering, is expected to have a flat spatial frequency dependent reflectance, and (b) the intensity scale, in terms of reflectance factor, was determined by measuring a 99% diffuse reflectance standard at zero spatial frequency and using its known reflectance factor in the measurement geometry (incident angle $\theta_i = 20°$ and scattering angle $\theta_s = 0°$) [15]. Thus, the data shown are given by

$$\mathbf{M}(f_y) = \mathbf{M}^{\text{meas}}(f_y) \times \frac{1.042 M_{11}^{\text{Al}}(0)}{M_{11}^{\text{Al}}(f_y) M_{11}^{R99}(0)}, \tag{1}$$

where $\mathbf{M}^{\text{meas}}(f_y)$, $\mathbf{M}^{\text{Al}}(f_y)$, and $\mathbf{M}^{\text{R99}}(f_y)$ are the measured Mueller matrices at spatial frequency f_y for the sample under test, the rough aluminum reference, and the diffuse reflectance standard, respectively. The diffuse reflectance standard is known to have a bidirectional reflectance factor of 1.042 at 630 nm in this geometry [15]. Mueller matrices are reported normalized as $m_{ij}(f_y) = M_{ij}(f_y) / M_{11}(f_y)$. Finally, MM decompositions [7] may enhance contrast for anisotropic samples, but none that we considered were particularly useful for the materials studied, since the MMs were nearly diagonal.

Images were cropped to contain the sample of interest, and no smoothing was applied. To avoid analyzing data dominated by noise, a Mueller matrix $\mathbf{M}(f_y)$ is discarded from analysis once the coefficient of variance of $M_{11}(f_y)$ is greater than 10%. For every experiment, the presented mean and standard deviation of the mean (expanded by $k = 2$) were taken from a 25 × 25 pixel region of interest (ROI). As expected, the Mueller matrix of the rough aluminum surface was found to be independent of f_y, while that of the diffuse reflectance standard showed weak dependence on f_y (reduced scattering coefficient 16.7 mm^{-1} [16]).

3. Examples

3.1 Intralipid sets for bulk phantoms

To investigate the sensitivity of Mueller matrix elements to absorption and scattering with structured illumination, bulk media measurements were performed with Intralipid (Fresenius-Kabi) to control scattering coefficient and Nigrosin (Sigma-Aldrich) to control absorption. A phantom matrix was made with three sets of reduced scattering coefficients μ_s' = (0.5,1.3,2.0) mm^{-1} and four sets of absorption coefficients μ_a = (0.00,0.25,0.50,0.75) mm^{-1}. Scattering was controlled by 20% volume dilutions of stock Intralipid with water according to

Biomedical Optics EXPRESS

empirical predictions [17], and absorption was controlled by making absorbance measurements of diluted Nigrosin to generate a prediction of μ_a with respect to concentration based upon the Beer-Lambert law. These 100 ml liquid phantoms were poured into a 6 cm × 6 cm black-anodized aluminum container, making them approximately 2.75 cm deep.

Since the Mueller matrix is largely diagonal and $m_{22} \cong -m_{33}$, only m_{22} and m_{44} are shown in Figs. 2 and 3. For the lowest scattering and absorption phantom, it should be noted that four repetitions were averaged instead of two, and the image noise was still problematic, such that any data from spatial frequencies higher than 0.5 mm^{-1} were discarded.

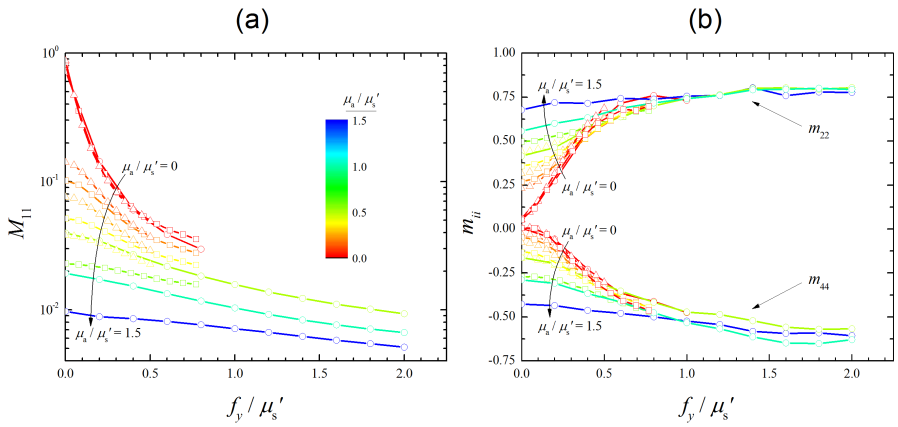

Fig. 2. Structured illumination Mueller matrix results from bulk Intralipid phantoms with varying optical properties for (a) M_{11} and (b) m_{22} and m_{44}. The reduced scattering coefficients are (circles) $\mu_s' = 0.5$ mm^{-1}, (squares) $\mu_s' = 1.3$ mm^{-1}, and (triangles) $\mu_s' = 2.0$ mm^{-1}. The color scale indicates the ratio μ_a / μ_s'. The standard deviations of the mean, not shown, are roughly as large as the symbols or smaller.

In Fig. 2, spatial frequency f_y is normalized by the reduced scattering coefficient μ_s', causing the non-absorbing samples (red curves) to be overlapping. However, the absorbing samples measured with planar illumination seen in Fig. 2 (at $f_y / \mu_s' = 0$) are dependent on both scattering and absorption, hence the highly stratified MM elements. The data in Fig. 2 is color-coded by the ratio μ_a / μ_s', illustrating that the behavior is well characterized by f_y / μ_s' and μ_a / μ_s'. In the diffuse regime ($f_y / \mu_s' < 0.33$) the curves for absorption are highly stratified, while in the sub-diffuse regime ($f_y / \mu_s' > 0.33$) [14] the curves approach a common value, representing the single-scattering behavior of the medium. The loss of sensitivity to absorption with increasing spatial frequency is an expected result for intensity measurements [14] and also helps to explain the increase in relative polarization with increased spatial frequency seen in Fig. 2(b). Just as increased absorption decreases the likelihood of multiple scattering events, so does increased spatial frequency, resulting in a lower degree of depolarization. We further notice that m_{44} has a slower response to increased spatial frequency (is much flatter) near $f_y / \mu_s' = 0$ compared to m_{22}, suggesting that depolarization does not occur uniformly for all initial polarization states. We look forward to investigating how various types of scatterers affect Mueller matrix elements differently, potentially for classification purposes [2,9].

If the spatial frequencies in Fig. 2 are not normalized by μ_s', these curves separate into groups based on the sample's scattering properties. To quantify if these phantoms statistically

Biomedical Optics EXPRESS

separate based on μ_s' and at what spatial frequency, a one-way analysis of variations (ANOVA) was done at each spatial frequency for each MM element using μ_s' as the factor. For M_{11}, m_{22}, and m_{44}, the resulting *p*-values with planar illumination (f_y = 0) are 0.95, 0.52, and 0.31, respectively, meaning there is no statistically significant separation using uniform illumination. If we consider a statistically significant separation to be a *p*-value of 0.05 (5% uncertainty), m_{22} and m_{44} *p*-values become less than 0.01 for spatial frequencies above 0.2 mm^{-1}. However, increased noise at the highest spatial frequencies ($\geq$ 0.9 mm^{-1}) increases this *p*-value above 0.05. The unpolarized reflectance m_{11} does not confidently separate the samples based on scattering properties until $f_y \geq$ 0.5 mm^{-1}. While this behavior for M_{11} has been previously demonstrated for unpolarized measurements [9], isolating samples based on their reduced scattering coefficient was achieved in this work at lower spatial frequencies using polarimetric elements. Lower spatial frequencies are generally easier to achieve with less noise and higher accuracy. Furthermore, this demonstrates that the presented system is more sensitive to scattering changes than SI or MMI alone.

3.2 Step phantom

To investigate potential depth sensitivity control for Mueller matrix elements using spatial frequency photon gating, the black-anodized aluminum container in the previous measurements was partially filled to control the phantom's depth in steps of 1 mm thickness from 1 mm to 5 mm. A diluted 20% Intralipid phantom with μ_a = 0.0 mm^{-1} and μ_s' = 0.5 mm^{-1} was used as the sample.

The depth phantom data is plotted versus the dimensionless spatial frequency f_y / μ_s' in Fig. 3 for unpolarized reflectance M_{11} (Fig. 3(a)) and for the linear and circular polarization components m_{22} and m_{44} (Fig. 3(b)), respectively. As shown in Fig. 3(a), the unpolarized reflectance at f_y / μ_s' = 0 is clearly separated by phantom depth, while the polarized elements (Fig. 3(b)) at f_y / μ_s' = 0 lose distinction past a depth of 3 mm. Because the only change between measurements is the phantom thickness, this stratification must be caused by optical sensing of the highly absorbing black aluminum substrate. As spatial frequency is increased, optical sensing depth becomes shallower and hence fewer photons reach the highly absorbing substrate. The shallow sensitivity causes all signals to converge in Fig. 3 at higher spatial frequencies, since the diffuse media are identical. Finally, the average photon path length decreases with increasing spatial frequency, leading to less depolarization. This effect is demonstrated in Fig. 3(b) as well as Fig. 2(b).

Biomedical Optics EXPRESS

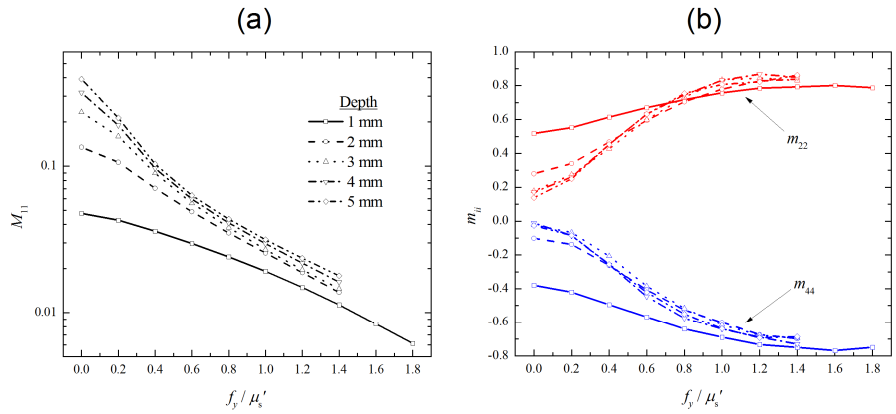

Fig 3. Structured illumination Mueller matrix results as a function of Intralipid phantom depth for (a) M_{11} and (b) m_{22} and m_{44}. The reduced scattering coefficient was $\mu_s' = 0.5\ \mathrm{mm}^{-1}$ and absorption coefficient was $\mu_a = 0$. The standard deviations of the mean, not shown, are roughly as large as the symbols or smaller.

3.3 Skin phantom

To demonstrate SI-MMI in an *ex vivo* sample, chicken breast skin was stretched over a capped petri dish 10 cm in diameter. Under the glass cap, the circular dish was separated into quadrants by alternating white and black paper (see Fig. 4). Characterized by their Lambertian reflectance and high absorption, they are labeled L and A, respectively. The average thickness of the skin as measured by calipers was 1.5 mm.

The *ex vivo* skin sample's Mueller matrix diagonal elements are traced over spatial frequency for the Lambertian (L) and high absorption (A) ROIs in Fig. 4(a). The ROIs are chosen manually to be close to each other so as to mitigate contrast due to spatial variations on the sample and close to the center of the image because the system calibration is based on the center optical axis. The MM values at low spatial frequency differ between the two substrates for each element, with the ROI over the high absorption backing having greater polarization due to the loss of deeply scattered, and therefore more depolarized photons. At spatial frequencies $f_y \geq 0.2\mathrm{mm}^{-1}$, this separation becomes negligible. In Fig. 4(b), M_{11} is mapped in greyscale with color bar on the left while normalized elements are mapped in red-blue with the color bar on the right. The substrate is clearly visible in $M_{11}(0)$, although it is seemingly masked by other features in $m_{22}(0)$ and $m_{44}(0)$. To get a better sense for the diffuse, deeply scattered photons, the bottom row of Fig. 4(b) shows $\Delta\mathbf{M} = \mathbf{M}(0) - \mathbf{M}\left(0.2\,\mathrm{mm}^{-1}\right)$. Here, each map displays a relatively clearer visualization of the substrate than the corresponding $f_y = 0$ map because surface scattering is removed. The scale for Δm_{22} and Δm_{44} is noticeably small, as most photons are depolarized, although contrast is still observed between the two substrates despite the sample thickness.

Biomedical Optics EXPRESS

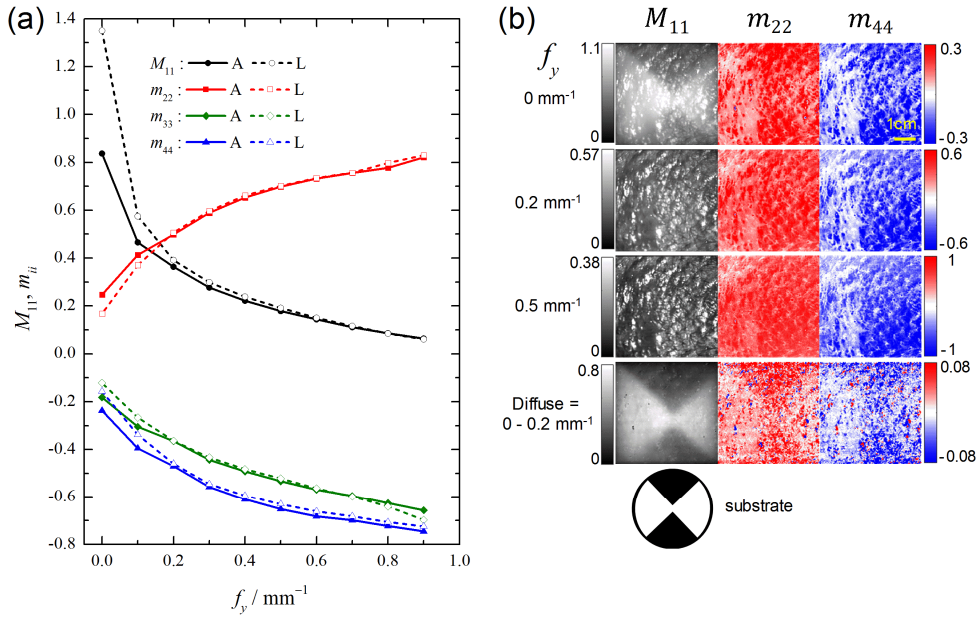

Fig. 4. Structured illumination Mueller matrix imaging results of the *ex vivo* chicken skin sample. In (a), ROI traces of the highly absorbing substrate (A – solid lines) and the Lambertian substrate (L – dotted lines) are shown. The standard deviations of the mean, not shown, are roughly as large as the symbols or smaller. In (b) M_{11}, m_{22}, and m_{44} images are shown for different spatial frequencies. The lowest row of images in (b) are derived from $\Delta\mathbf{M}$, as described in the text. A 1 cm scale bar is shown in the upper right image.

4. Summary and conclusion

In this letter, we investigate the capabilities of SI-MMI to control average photon path lengths and demonstrated its effects on polarization parameters. Imaging of tissue phantoms showed increased sensitivity to scattering parameters and shallower depths with increasing spatial frequency. Furthermore, polarimetry parameters were more sensitive than that of unpolarized intensity to changes in scattering. This technique was further demonstrated on an *ex vivo* chicken skin sample, showing a loss of sensitivity to a deep substrate layer with increasing spatial frequency.

Controlling photon path length with SI can lead to a loss of sensitivity to deeper layers of the sample, as demonstrated in Fig. 3 and 4. Standard wide-field MMI could be sensitive to layers beyond the surface of interest, yet with increased spatial frequency the Intralipid depth phantom and the skin sample show negligible sensitivity to the absorbing substrates. In the future, we would like to investigate the depth dependence of SI-MMI in finer depth resolution [18].

The current system is not optimized for speed and takes approximately 1 hour to acquire a full spatial frequency sweep for a given sample. Much of this excess time is due to the outdated camera used in this study. We are currently installing a modern camera; imaging at 24 frames per second with fast image acquisition should reduce the acquisition time to 44 s. However, both the SI and MMI fields have developed snapshot techniques seemingly amenable to combination [19,20]. Furthermore, a full sweep of spatial frequency may not be necessary.

Many potential synergies could develop between the fully described light scattering of MMI and practical implementation of SI. Future work will expand upon the quantitative capabilities of both SI and MMI techniques into this single new imaging modality.

Biomedical Optics EXPRESS

Disclosures

The authors declare that there are no conflicts of interest related to this article.

Certain materials are identified in this paper in order to specify the experimental procedure adequately. Such identification is not intended to imply recommendation or endorsement by the National Institute of Standards and Technology, nor is it intended to imply that the materials or equipment identified are necessarily the best available for the purpose.

References

1. S. Alali and A. Vitkin, "Polarized light imaging in biomedicine: emerging Mueller matrix methodologies for bulk tissue assessment," J. Biomed. Opt. **20**(6), 061104 (2015).
2. A. Hielscher, A. Eick, J. Mourant, D. Shen, J. Freyer, and I. Bigio, "Diffuse backscattering Mueller matricesof highly scattering media," Opt. Express **1**(13), 441–453 (1997).
3. M. K. Swami, S. Manhas, H. Patel, and P. K. Gupta, "Mueller matrix measurements on absorbing turbid medium," Appl. Opt. **49**(18), 3458–3464 (2010).
4. M. Sun, H. He, N. Zeng, E. Du, Y. Guo, S. Liu, J. Wu, Y. He, and H. Ma, "Characterizing the microstructures of biological tissues using Mueller matrix and transformed polarization parameters," Biomed. Opt. Express **5**(12), 4223–4234 (2014).
5. I. Ahmad, M. Ahmad, K. Khan, S. Ashraf, S. Ahmad, and M. Ikram, "*Ex vivo* characterization of normal and adenocarcinoma colon samples by Mueller matrix polarimetry," J. Biomed. Opt. **20**(5), 056012 (2015).
6. A. Pierangelo, S. Manhas, A. Benali, C. Fallet, M.-R. Antonelli, T. Novikova, B. Gayet, P. Validire, and A. De Martino, "*Ex vivo* photometric and polarimetric multilayer characterization of human healthy colon by multispectral Mueller imaging," J. Biomed. Opt. **17**(6), 066009 (2012).
7. S.-Y. Lu and R. A. Chipman, "Interpretation of Mueller matrices based on polar decomposition," J. Opt. Soc. Am. A **13**(5), 1106 (1996).
8. J. F. de Boer, C. K. Hitzenberger, and Y. Yasuno, "Polarization sensitive optical coherence tomography - a review," Biomed. Opt. Express **8**(3), 1838–1873 (2017).
9. N. Bodenschatz, P. Krauter, A. Liemert, and A. Kienle, "Quantifying phase function influence in subdiffusively backscattered light," J. Biomed. Opt. **21**(3), 035002 (2016).
10. B. Yang, J. Lesicko, M. Sharma, M. Hill, M. S. Sacks, and J. W. Tunnell, "Polarized light spatial frequency domain imaging for non-destructive quantification of soft tissue fibrous structures," Biomed. Opt. Express **6**(4), 1520–1533 (2015).
11. A. De Martino, Y.-K. Kim, E. Garcia-Caurel, B. Laude, and B. Drévillon, "Optimized Mueller polarimeter with liquid crystals," Opt. Lett. **28**(8), 616–618 (2003).
12. E. Compain, S. Poirier, and B. Drevillon, "General and self-consistent method for the calibration of polarization modulators, polarimeters, and Mueller-matrix ellipsometers," Appl. Opt. **38**(16), 3490–3502 (1999).
13. J. P. Angelo, S.-J. Chen, M. Ochoa, U. Sunar, S. Gioux, and X. Intes, "Review of structured light in diffuse optical imaging," J. Biomed. Opt. **24**(7), 1–20 (2018).
14. D. J. Cuccia, F. Bevilacqua, A. J. Durkin, F. R. Ayers, B. J. Tromberg, and J. Bruce, "Quantitation and mapping of tissue optical properties using modulated imaging," J. Biomed. Opt. **14**(2), 024012 (2009).
15. T. A. Germer, "Full four-dimensional and reciprocal Mueller matrix bidirectional reflectance distribution function of sintered polytetrafluoroethylene," Appl. Opt. **56**(33), 9333–9340 (2017).
16. Q. Li, B. J. Lee, Z. M. Zhang, and D. W. Allen, "Light scattering of semitransparent sintered polytetrafluoroethylene films," J. Biomed. Opt. **13**(5), 054064 (2008).
17. P. D. Ninni, F. Martelli, and G. Zaccanti, "Intralipid: towards a diffusive reference standard for optical tissue phantoms," Phys. Med. Biol. **56**(2), N21–N28 (2011).
18. C. K. Hayakawa, K. Karrobi, V. Pera, D. Roblyer, and V. Venugopalan, "Optical sampling depth in the spatial frequency domain," J. Biomed. Opt. **24**(7), 1–14 (2018).
19. J. P. Angelo, M. van de Giessen, and S. Gioux, "Real-time endoscopic oxygenation imaging using single snapshot of optical properties (SSOP) imaging," in B. W. Pogue and S. Gioux, eds. (International Society for Optics and Photonics, 2016), p. 969605.
20. J. Qi, C. He, and D. S. Elson, "Real time complete Stokes polarimetric imager based on a linear polarizer array camera for tissue polarimetric imaging," Biomed. Opt. Express **8**(11), 4933–4946 (2017).